# Degradation Mechanism of Metal–Organic Framework Drug Nanocarriers Studied by Solid-State Nuclear Magnetic Resonance and X-ray Absorption Near-Edge Structure Spectroscopy

Dang Le Mai Vuong, Ioanna Christodoulou, Marianna Porcino, Sĩ Thành Đồng, Benedikt Lassalle-Kaiser, Mohamed Haouas, Ruxandra Gref, Charlotte Martineau-Corcos

# Degradation mechanism of metal-organic framework drug nanocarriers studied by solid-state NMR and XANES spectroscopy

*Mai Dang Le Vuong[1,2], Ioanna Christodoulou[2,a], Marianna Porcino[3], Si-Thanh Dong[4], Benedikt Lassalle-Kaiser[4], Mohamed Haouas[1], Ruxandra Gref[2], and Charlotte Martineau-Corcos[1,b]*

AUTHOR ADDRESS

(1) Université Paris-Saclay, UVSQ, CNRS, Institut Lavoisier de Versailles, 78000, Versailles, France

(2) Université Paris-Saclay, CNRS, Institut des Sciences Moléculaires d'Orsay, 91405, Orsay, France

(3) Université d'Orléans, CNRS, Conditions Extrêmes et Matériaux : Haute Température et Irradiation (CEMHTI), CNRS UPR 3079, 45071, Orléans, France

(4) Synchrotron SOLEIL, 91192, L'Orme des Merisiers, Gif-sur-Yvette, France

ABSTRACT. Metal-organic framework nanoparticles (nanoMOFs) are novel porous drug delivery systems whose features include high drug loading capacity, versatile functionalization, biocompatibility, and biodegradability. However, little knowledge about the nature of nanoMOFs degradation mechanism is one of many reasons that prevents their clinical use. MIL-100 (MIL stands for Matériaux de l'Institut Lavoisier) is among the most studied nanoMOF for drug delivery. Here, we investigate at the atomic scale the degradation mechanism of metal(III)-trimesate nanoMIL-100 drug carrier in biological-mimicking phosphate medium. By using solid-state NMR (ssNMR) spectroscopy, we found that the first step of nanoMIL-100(Al) degradation is the substitution of labile water ligands, resulting in new coordination bonds between Al(III) and phosphate ions, followed by the substitution of trimesate ligands leading to their release. The data indicated that the reaction-limiting step most likely is the formation of an inorganic aluminophosphate layer at the nanoparticle surface and that drug encapsulation and surface coating affect the nanoMIL-100(Al) degradation. X-ray Absorption Near Edge Structure (XANES) spectroscopy study of nanoMIL-100(Fe) degradation corroborates the hypothesized alteration mechanism of nanoMIL-100(Al). From the ensemble of data, a stepwise degradation mechanism representative for the nanoMIL-100 drug delivery system is proposed.

## 1. Introduction

The concept of sustained drug release has been around since the 1960s[1]; the quest has never stopped to search for the most appropriate drug carriers for the delivery and controlled release of therapeutic molecules to a targeted location in the patient. Since the first report in 2010[22], metal-organic framework nanoparticles (nanoMOFs) as drug carriers have gained increasing interest as they combine the advantages of both their inorganic and organic constituents. Metal-organic

frameworks (MOFs) are porous materials made of metal-ligand coordination units assembled as an ordered crystalline structure with high permanent porosity[3-5]. This high porosity enables MOFs to capture a large amount of drug within a small amount of carrier, thus potentially reducing the administered dose and related toxicity for the patients.

Among the most studied nanoMOFs for drug delivery to date is nanoMIL-100(Fe), belonging to the MOF family of MIL-100. It consists of trivalent metal cations such as Al (III) or Fe (III), and benzene-1,3,5-tricarboxylate ligands, also called trimesate or BTC[6,7]. **Figure 1** illustrates the structure of MIL-100. Its secondary building unit (SBU), the Fe or Al(III) metal trimer, consists of three metal cations (III) coordinated with one central bridging oxygen and six carboxylate groups. The 6-fold coordination sphere is completed with hydroxyl and water ligands. Two metal cations coordinate with one water molecule per cation, and one cation coordinates with one hydroxyl group. Every four SBUs connect through trimesate linkers, creating tetrahedra. These tetrahedra build the MTN type MIL-100 framework, which possesses two kinds of pores: large mesoporous cages of 29 Å diameter, accessible through hexagonal (8.6 Å) and pentagonal windows (4.8-5.5 Å), and small mesoporous cages of 25 Å diameter, accessible exclusively through pentagonal opening windows. The generally accepted formula is $M_3O(H_2O)_2OH(C_6H_3(CO_2)_3)_2$ (M is Fe or Al)[7,8]. In addition, the MIL-100 MOFs consist of coordinative unsaturated metal sites (CUS) with strong Lewis acid properties produced upon thermal activation and departure of labile ligands[9,10].

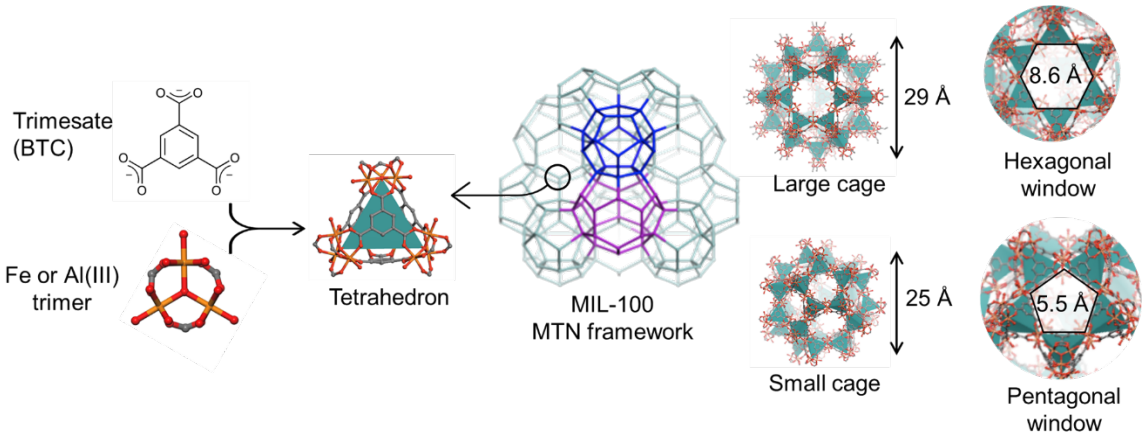


**Figure 1.** Structure of the MOF family MIL-100. The Fe(III) or Al(III) trimer is 6-coordinate Fe or Al (III) coordinating with bridging oxygen, water, trimesate, and hydroxyl ligands. Tetrahedra, made of Fe or Al(III) trimers on their vertices and trimesates on their faces, are arranged following the MTN framework, creating two types of mesoporous cages: large cages with 29 Å diameter, accessible through hexagonal (8.6 Å) and pentagonal windows (4.8-5.5 Å), and small cages with 25 Å diameter, accessible only through pentagonal windows. Adapted from reference[11].

The high drug payload of nanoMIL-100(Fe) has been demonstrated for various drugs[12,1312,13], namely anticancer[2,14,15], antibiotic[16,17], antiretroviral[18], and a combination of anti-inflammatory and antibiotics[19]. For example, the anticancer drug busulfan was loaded in nanoMIL-100(Fe) with a payload of 25 wt%, five and sixty times higher than its payload in polymer nanoparticles and in liposomes, respectively[2,20,21]. Recently, the aluminum-trimesate nanoMIL-100(Al) was also explored for drug delivery. The MIL-100(Al) gel loaded with the anticancer drug doxorubicin (DOX) showed a remarkably high payload of 62 wt%[22]. More recently, DOX was efficiently encapsulated (74% encapsulation efficiency) in core-shell nanoMIL-100(Al) coated with γ-cyclodextrin (CD) citrate and was released progressively depending on the initial drug loading[23].

Both nanoMIL-100(Al) and nanoMIL-100(Fe) demonstrated high loading capacity for active molecules bearing phosphate moieties because of the strong interaction between Al(III) or Fe(III) CUS and phosphate group[14,18,24]. Additionally, to improve the nanoMOF's colloidal stability and to modulate their interaction with biological media and cells, the surface of nanoMIL-100(Fe) and nanoMIL-100(Al) was coated covalently with polymers[25] or non-covalently with biopolymers, lipids and carbohydrates[15,26-31]. More importantly, for biomedical applications, nanoMIL-100(Fe) has been shown non-toxic and biodegradable *in vitro*[2,32,33] and *in vivo*[2,21,34,35]. NanoMIL-100(Al) has also been shown non-toxic *in vitro*[33]. Still, many questions remain about the nanoMIL-100 carrier stability, for instance, toxicity might come from nanoMOF's degradation products[32] or drug encapsulation can modify nanoMOF's degradation kinetics[21]. To further progress the clinical translation of nanoMOFs, a critical aspect that needs to be addressed is deciphering the degradation mechanism of the nanoMIL-100 family.

However, there is little literature on the important topic of nanoMIL-100 degradation in biological-relevant media and the effects of drug encapsulation and surface coating. A popular hypothesis is that the degradation reaction of MIL-100(Fe) produces free iron(III) ions and trimesic acid. Early studies found that the culprit of degradation is the phosphate component of the cell medium[18,36]. The higher the phosphate concentration, the higher the trimesate release, the more degraded the nanoMOF[16]. Li *et al*. discovered that despite witnessing more than 30% trimesate ligand loss, the MIL-100(Fe) nano- and micro-particles maintained their sizes and shapes upon exposure to phosphate buffer[37]. Using Raman and Mossbauer spectroscopy, the authors suspected the formation of an amorphous shell of iron phosphate and/or iron oxide surrounding an intact crystalline core. In addition, using *in situ* atomic force microscopy and high-resolution transmission electron microscopy, Christodoulou *et al*. also found that the nanoMIL-100(Fe) and

microMIL-100(Fe) degraded without collapsing or changing their dimension[1111]. Degradation of MIL-100(Fe) started at the particle surface, where the crystal planes at the surface disappeared within 2 hours of incubation in phosphate buffer saline (PBS) at pH 7.4. However, none of these techniques have given evidence at the atomic scale for the changes in iron coordination.

To study the MOF structure at the atomic scale, solid-state NMR (ssNMR) spectroscopy is a non-destructive and valuable technique to get information about both the long-range crystal structure (when combined with XRD and periodic first-principles calculations)[38] and short-range local structure or interactions in MOFs. Deviations from periodic structures in MOFs can happen after chemical modification or functionalization, which are often not detected by routine characterization techniques such as X-ray diffraction and infrared spectroscopy. In this case, ssNMR spectroscopy is a technique of choice for locally probing atoms, their neighboring environments, and chemical bonds while keeping the MOF intact[39,40]. It has been used extensively to determine the structure of new MOFs[7,41,42], and the adsorption-desorption mechanism of liquid and gases[43,44]. For porous drug delivery systems, ssNMR spectroscopy has been mainly used to study mesoporous silica[45-47] and MOFs[48,49]. For MIL-100(Fe), ssNMR spectroscopy gave indirect proof about the interaction between the strong paramagnetic Fe(III) and the drug azidothymidine triphosphate or the coating cyclodextrin phosphate (CD-P)[18,26]. For diamagnetic MIL-100(Al), ssNMR spectroscopy provided insights about host-guest interaction and location of the drugs adenosine triphosphate (ATP) and doxorubicin, as well as the surface coating cyclodextrin-phosphate (CD-P)[23,24].

In this work, we further use solid-state NMR spectroscopy to investigate the degradation mechanism at the atomic scale of this nanoMIL-100(Al) in PBS, revealing a stepwise degradation process. We also study the impact of ATP drug loading and CD-P surface modification on the

nanoMOF degradation. ATP and CD-P were chosen based on their well-known interaction between molecules bearing phosphate moieties and the Al(III) cations of nanoMIL-100(Al)[24,26]. The ensemble of ssNMR data ($^{27}$Al, $^{31}$P, $^{31}$P-$^{27}$Al) reveals the evolution of the metal coordination sphere in MIL-100 during degradation reaction, as a function of several parameters: MIL-100 structure, concentration of the degradation medium, interaction with surface coating and loaded drug. To check whether our proposed degradation mechanism applies to the iron MIL-100 analog, we studied the degradation of nanoMIL-100(Fe) in PBS by XANES spectroscopy, which was selected because it can provide information about the local structure of iron(III) in MOFs[50,51]. This paper shows that using a combination of ssNMR and XANES spectroscopy allows better understanding of the chemistry of nanoMIL-100 drug carriers and their degradation.

## 2. Experimental Section

Herein the most important experimental methods and techniques are summarized. Details are given in the Supporting Information.

### 2.1. Synthesis of nanoMIL-100(Al) and nanoMIL-100(Fe)

NanoMIL-100(Al) and nanoMIL-100(Fe) were synthesized by microwave-assisted synthesis, following a published procedure[8,52]. All reagents and solvents were used without further purification.

### 2.2. Drug encapsulation and surface coating of nanoMIL-100(Al)

NanoMOFs were loaded with ATP with the input loading 30 wt% of initial nanoMOF, following a reported soaking procedure[14]. A 1.5 mg.mL$^{-1}$ aqueous solution of ATP disodium salt hydrate was added to a determined milligram of nanoMOF (m_MOF). The final nanoMOF concentration was 5 mg.mL$^{-1}$. The weight of drug remaining in the supernatant after drug loading

145 (m_drug_remaining) was determined by HPLC based on a reported procedure[53]. The actual drug
146 payload wt% was calculated as: $\frac{\text{m\_drug\_input} - \text{m\_drug\_remaining}}{\text{m\_MOF}} \times 100$, where m_drug_input is the
147 weight of drug added to nanoMOF.
148 NanoMOFs were coated with phosphate-β-cyclodextrin (CD-P) at the theoretical coating 30
149 wt% of initial MOF, by adapting a published method[26]. A 3 $mg.mL^{-1}$ aqueous solution of
150 phosphated β-cyclodextrin CD-P sodium salt (average 3-4 phosphate groups per cyclodextrin unit)
151 was added to a determined milligram of nanoMOF. The final nanoMOF concentration was 10
152 $mg.mL^{-1}$. The amount of coating remaining in the supernatant after surface coating
153 (m_coating_remaining) was determined by quantitative liquid-state NMR spectroscopy. The
154 actual surface coating wt% was calculated as: $\frac{\text{m\_coating\_input} - \text{m\_coating\_remaining}}{\text{m\_MOF}} \times 100$, where
155 m_coating_input is the weight of drug added to nanoMOF.
156 2.3.Degradation of nanoMIL-100(Al) and nanoMIL-100(Fe)
157 NanoMOF was incubated in PBS pH 7.4 at 37°C for 2-5 days following two conditions: 10
158 $mg.mL^{-1}$ nanoMOF and PBS 10 mM, and 0.5 $mg.mL^{-1}$ nanoMOF and PBS 1 mM. PBS used is
159 Dulbecco's Phosphate-Buffered Saline 1X *i.e.*, 10 mM, pH 7.0-7.3, comprised of 8.1 mM
160 $Na_2HPO_4$, 1.5 mM $KH_2PO_4$, 138 mM NaCl, and 2.7 mM KCl.
161 2.4. Characterization of nanoMIL-100(Al)
162 Morphology and size of nanoMOF were observed by Transmission Electron Microscopy (TEM)
163 under a 120 kV microscope. Particle size of 0.5 $mg.mL^{-1}$ nanoMOF suspension in EtOH abs or
164 deionized (DI) water was measured by Dynamic Light Scattering (DLS). Specific surface area of
165 MOF was measured by the Brunauer–Emmett–Teller technique (BET) after degassing MOF
166 powder under vacuum at 100°C overnight. Crystallinity was evaluated by performing Powder X-
167 ray Diffraction (PXRD) at λ(Cu Kα) of 1.5406 Å. Thermal stability was studied by

Thermogravimetric Analysis (TGA). The amount of trimesate and ATP in the supernatant collected after nanoMOF degradation was determined by High-Performance Liquid Chromatography (HPLC) following a published procedure[37]. The amount of CD-P in the supernatant was determined by NMR spectroscopy, performed at 9.4 T on a Bruker Avance spectrometer equipped with a probe head of 5 mm. The chemical shifts were referenced to tetramethylsilane for $^{1}H$ and $^{13}C$. Coordination structure of nanoMIL-100(Fe) was studied by XANES spectroscopy recorded at the K-edge of Fe at 7112 eV at the SAMBA beamline in Synchrotron SOLEIL, France. Experimental details are reported in the Supporting Information (SI).

Coordination structure of nanoMIL-100(Al) was studied by Magic-Angle Spinning (MAS) NMR spectroscopy performed at 11.7 T on a Bruker NEO NMR WB spectrometer equipped with probe heads of 4 and 3.2 mm, except for the $^{31}P$-$^{27}Al$ 2D NMR measurement, which was recorded at 17.6 T with a 4 mm probe head. The chemical shifts were referenced to tetramethylsilane for $^{1}H$ and $^{13}C$, to $Al(NO_3)_3$ 1 M solution for $^{27}Al$, and to $H_3PO_4$ 85 wt% solution for $^{31}P$. **Table S1** in SI reports details of NMR experiments.

## 3. Results and Discussion

### 3.1. Preparation and characterization of nanoMIL-100(Al)

The first step of this study was the synthesis of nanoMIL-100(Al) suspensions adequate as drug carriers, *i.e.* having a diameter lower than 200 nm and uniform size distribution. However, following a published procedure[52], the obtained MIL-100(Al) suspension had an inhomogeneous size distribution. Therefore, we used an additional size separation step and successfully prepared nanoMIL-100(Al) with hydrodynamic diameter Z-Average of 147 ± 14 nm and polydispersity

191 index PdI of 0.10 ± 0.02 (**Figure S1)**. TEM images (**Figure 3**a and **Figure S2**) also displayed solid
192 nanoMIL-100(Al) particles with uniform shape and size (88 ± 25 nm). The nanoparticle size was
193 overestimated by DLS because in DLS, the average nanoparticle diameter is determined from
194 scattered light intensity and large objects scatter more light than small ones[54]. The chemical
195 composition of the obtained nanoMIL-100(Al) was analyzed by TGA (**Figure S4**). It also showed
196 good crystallinity (XRD pattern in **Figure S5**) and a BET surface area of 1770 $m^2.g^{-1}$ ($N_2$
197 adsorption isotherm in **Figure S3a)**, which agree with published studies of MIL-100(Al)[7,52]. $^{1}H$
198 and $^{13}C$ MAS NMR spectra in **Figure S6** and **Figure S7** show typical features for MIL-100(Al)
199 materials.

200 A recent study by our group detected an extra $^{27}Al$ peak in MIL-100(Al) nanoparticle, which
201 was not detected in the previous study of MIL-100(Al) microparticle[7]. This extra peak represents
202 the surface Al sites in MIL-100(Al) nanoparticle, indicated by high field NMR experiments $^{31}P$-
203 $^{27}Al$ *D*-HMQC and $^{27}Al$ 2D MQMAS[24]. These surface species were reproduced in this study
204 (**Figure S8**) and are expected to play a crucial role in the degradation of nanoMIL-100(Al).

205 3.2. Degradation mechanism of nanoMIL-100(Al)

206 In the second step of this study, nanoMIL-100(Al) was incubated in PBS, composed of
207 phosphate monobasic and dibasic salts, at 37°C to mimic the physiological medium. All
208 measurements were performed *ex situ* by recovering the nanoparticles from suspension in PBS
209 after a given degradation period.

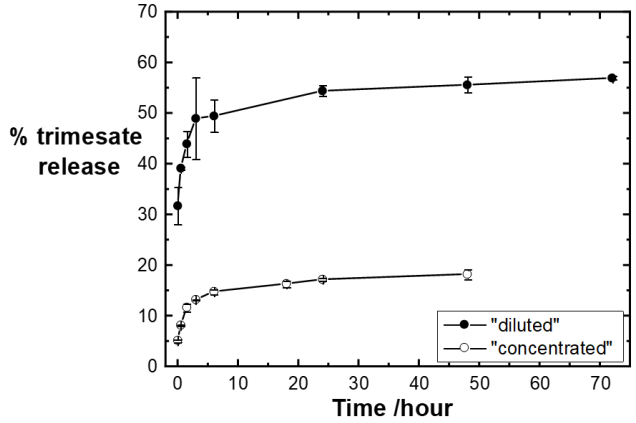


**Figure 2**. Kinetics of trimesate release, represented by the proportion of trimesate detected in the supernatant after degradation over the initial trimesate content in nanoMIL-100(Al). Two degradation conditions were named "diluted": 0.5 mg.mL$^{-1}$ MOF in PBS 1 mM, and "concentrated": 10 mg.mL$^{-1}$ MOF in PBS 10 mM, respectively.

As a first step, to choose the suitable conditions for the NMR investigation, we determined the degradation kinetics of nanoMIL-100(Al) and the formation of trimesate by using HPLC. We chose two degradation conditions, “concentrated”:10 mg.mL$^{-1}$ nanoMIL-100(Al) in PBS 10 mM, 2 days, and “diluted”: 0.5 mg.mL$^{-1}$ nanoMIL-100(Al) in PBS 1 mM, 2 days. In the “concentrated” condition, the molar ratio of phosphate/$Al_3$ trimer (P/$Al_3$) is 0.54:1, meaning that nanoMIL-100(Al) is in excess, whereas in the “diluted” condition, the P/$Al_3$ is 11:1, and PBS is in excess compared to nanoMIL-100(Al). The percentage of released trimesate upon degradation in PBS is shown in **Figure 2**. As expected, the release profile of trimesate from nanoMIL-100(Al) had a similar pattern with MIL-100(Fe) and consisted of two stages. In the first three hours after incubation in PBS, there was a rapid generation of trimesic acid. Subsequently, the degradation reaction rate decreased gradually in the next 24 hours and reached equilibrium after 48-72 hours. This plateau of trimesate release after a given period was also observed in other works dealing with MIL-100(Fe)[11,16,18].

227 There could be two explanations for this degradation plateau: 1) insufficient amount of
228 phosphate to react with nanoMIL-100(Al), or 2) another mechanism preventing the reaction from
229 proceeding further. The first explanation was supported by the fact that the trimesate release was
230 higher in the "diluted" degradation, where the ratio $P/Al_3$ was higher than in the "concentrated"
231 degradation. To investigate further the limitation step of the nanoMIL-100 degradation reaction,
232 the morphology and structure of the degraded nanoMOF were characterized.

233 Modification of nanoMIL-100(Al) morphology after 48-hour degradation is shown in **Figure**
234 **3b** and **Figure S9**. The degraded nanoMIL-100(Al) retained their initial faceted shape and size
235 distribution 98 ±24 nm, similar to the degraded nanoMIL-100(Fe) in Li *et al.*[37]. However, the
236 degraded nanoMIL-100(Al) had holes on its surface, which is somewhat different from the
237 degraded nanoMIL-100(Fe), whose TEM images displayed particles with rounded edges and
238 without holes at the surface.

239

240

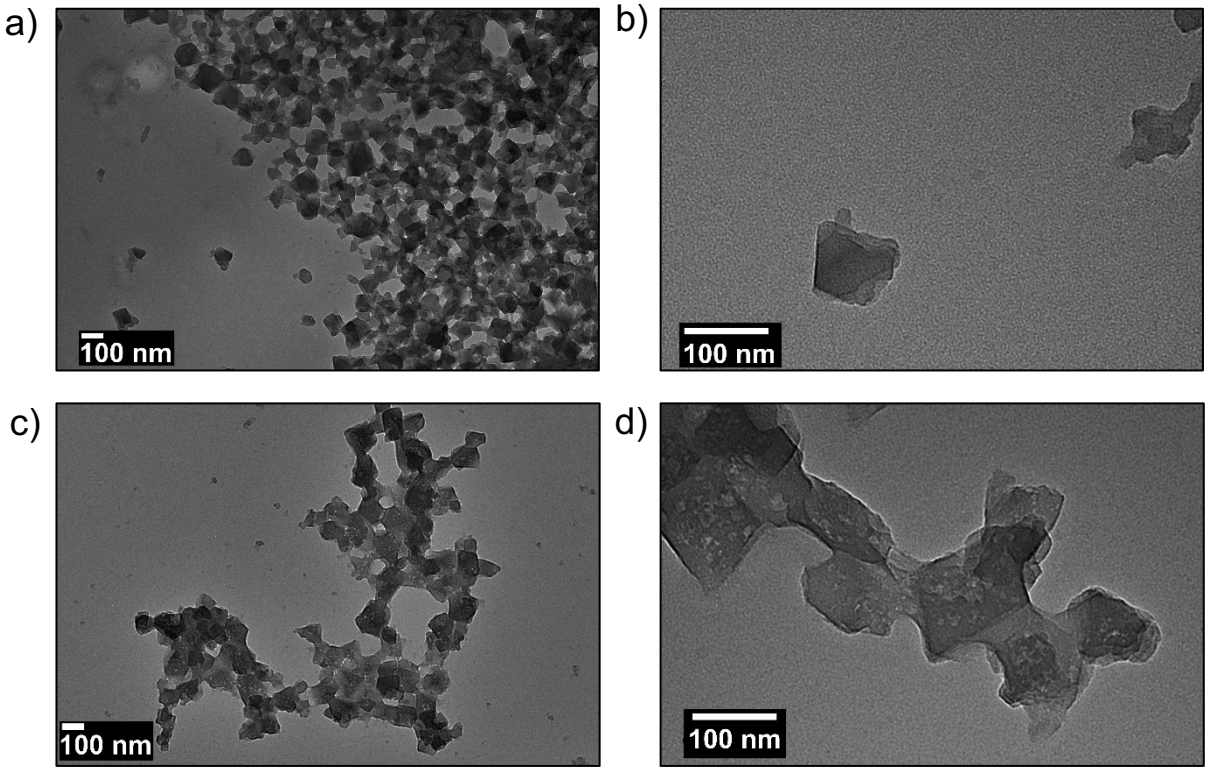


**Figure 3.** TEM images of intact nanoMIL-100(Al) at 10 k (a) and 30 k (b) magnification. TEM images of degraded nanoMIL-100(Al) at 10 k (c) and 30 k (d) magnification. Degradation was carried out with "diluted" condition: 0.5 mg.mL$^{-1}$ nanoMOF in PBS 10 mM.

More importantly, solid-state NMR spectroscopy demonstrates significant changes in the coordination sphere of nanoMIL-100(Al) after 48-hour degradation, indicated by the evolution of $^{27}$Al MAS NMR spectra (**Figure 4a**). The first noticeable change is the growth of the $^{27}$Al resonance around –2 ppm, a chemical shift characteristic of 6-coordinate Al cations coordinated to phosphate ions, coming from the MIL-100(Al) trimer and the degradation medium PBS, respectively. The presence of this new coordination mode for the 6-fold aluminum was confirmed in the $^{27}$Al multiple-quantum MAS (MQMAS) NMR spectrum of the degraded nanoparticles (**Figure 5**). The formation of the Al-O-P bond was further evidenced by the $^{31}$P-$^{27}$Al 2D MAS NMR spectrum (**Figure 4b**), which showed a correlation peak between this $^{27}$Al resonance at –2

ppm and the $^{31}P$ resonances around –10 ppm. This $^{31}P$-$^{27}Al$ correlation peak indicates close spatial proximity within 5 Å between these two nuclei, which fits the Al-O-P bond distance. It was also confirmed by $^{1}H$-$^{31}P$ and $^{1}H$-$^{27}Al$ 2D NMR spectroscopy (**Figure S12** and **Figure S13**), showing, in the degraded MIL-100(Al), the proximity between the phosphorus and the protons of the linker, and between the new 6-coordinate Al(III) and the trimesate linker. Note that this degraded Al species still remains in 6-coordination state as in the original MIL-100(Al) trimer, indicating that substitution of an existing ligand such as water or trimesate occurred. Trimesate is a stronger Lewis base than water, thus the metal-ligand bond Al-O-H between Al(III) and water is more easily broken than the metal-ligand bond Al-O-C between Al(III) and trimesate. As a result, phosphate ions from PBS should first replace the water ligand and form a strong Al-O-P coordination bond with Al(III) center. Then, due to an increase in interaction between the Al metal center and the newly bonded phosphate ligand, interaction of the Al center with the trimesate ligands decreases. As the connection Al-O-C between carboxylic groups of the trimesate and Al weakens, phosphate can also attack and replace the position of carboxylate. Free trimesic acid is liberated when all 6 Al-O-C bonds between a trimesate linker and Al trimers are disconnected.

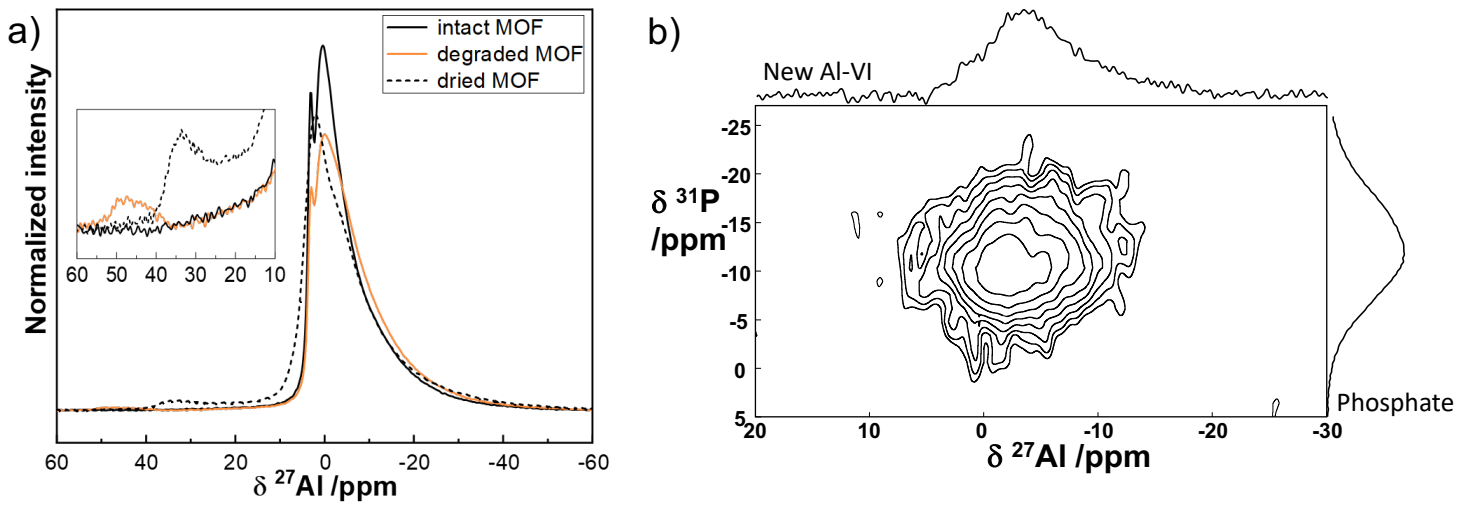


271 **Figure 4.** a) $^{27}$Al MAS NMR spectrum of intact (solid black line), degraded (orange), and
272 dehydrated (black dash line) nanoMIL-100(Al). The inset graph shows the 40 ppm region
273 corresponding to the 4 and 5-coordinate Al(III). b) 2D $^{31}$P-$^{27}$Al MAS NMR spectrum of degraded
274 MOF in excess PBS.

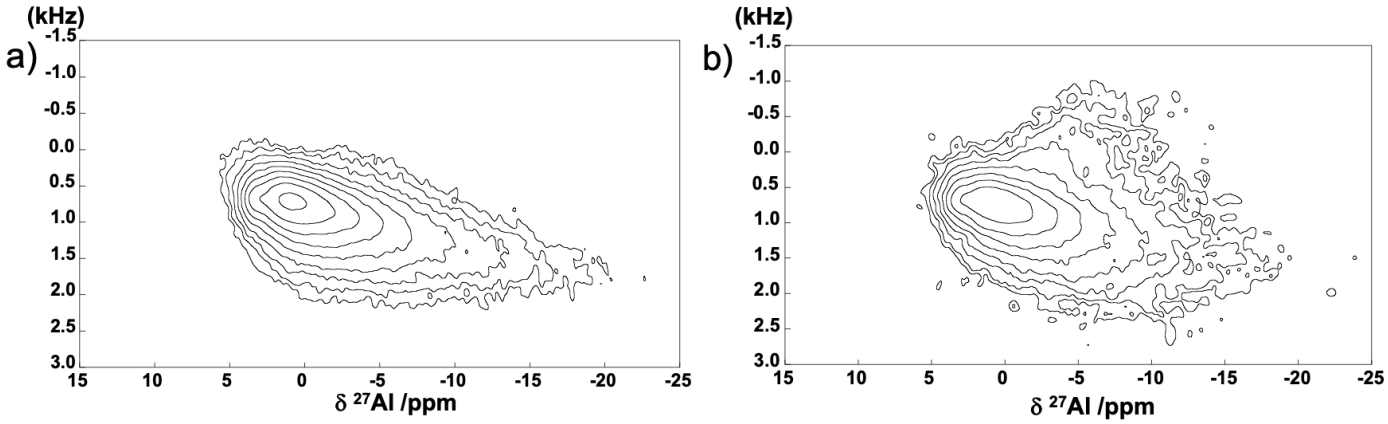


275

276 **Figure 5.** $^{27}$Al MQMAS spectrum of a) original and b) degraded nanoMIL-100(Al)

277

278 Notably, the 1D $^{27}$Al MAS NMR spectrum of the degraded nanoMIL-100(Al) (**Figure 4**) shows
279 another new Al species at 48 ppm, whose chemical shift lies between the range of 4- and 5-
280 coordinate aluminum cations. A decrease in the coordination number of aluminum cations in MIL-

100(Al) is a known phenomenon observed when heating the sample above 150°C. As in the study of Haouas *et al*.[55], we also found that the coordinated water ligands were removed by heating, thus creating 5-coordinate Al cations with a $^{27}$Al chemical shift of 34 ppm (**Figure 4**). When the dehydrated MIL-100(Al) re-adsorbed water from ambient air, this 5-coordinate Al cation returned to 6-fold coordination without modifying the framework. However, in the degraded MIL-100(Al), the degraded low-coordinate Al had a higher chemical shift of 48 ppm; and this chemical shift did not change when the sample was exposed to air or heated above 150°C (**Figure S11**), implying that this low-coordinate Al site no longer coordinates with water ligands. As Al(III) species bonded with phosphate usually have lower $^{27}$Al chemical shifts than the same coordination number Al(III) species with no phosphate ligand due to a deshielding effect in NMR[56], we hypothesize that these Al species at 48 ppm are 4-coordinate Al with at least one phosphate ligand. Such 4-coordinate-Al is favorable in basic pH but not in neutral pH of PBS[56], which could explain why these species have very low intensity in the $^{27}$Al NMR spectrum. When the nanoMIL-100(Al) was degraded in excess PBS ("diluted" condition), the intensity of the 4-coordinate $^{27}$Al peak increased slightly, and even a new 5-coordinate $^{27}$Al peak was observed around 22-25 ppm (**Figure 6**). Therefore, we ruled out the possibility of an intermediate product, and we assigned these 4- and 5-coordinate $^{27}$Al resonances to an inorganic aluminum phosphate $AlPO_4$[58,5957,58]. As the 4- and 5-coordinate $^{27}$Al peaks only account for 1% of the total Al amount, the amount of these degradation products is low, and their formation may happen only at the surface. If these 4- and 5-coordinate aluminophosphate form a non-porous layer, this layer can passivate the nanoMIL-100(Al) surface, prevent phosphate from reacting with nanoMIL-100(Al), thus slowing down the degradation reaction. Blocked access to the nanoMIL-100(Al) was supported by a 10-time decrease in BET surface area (**Figure S3**).

The existence of this passivation layer may explain how degradation and trimesate release reached a plateau after 48 hours as determined by HPLC (**Figure 2**).

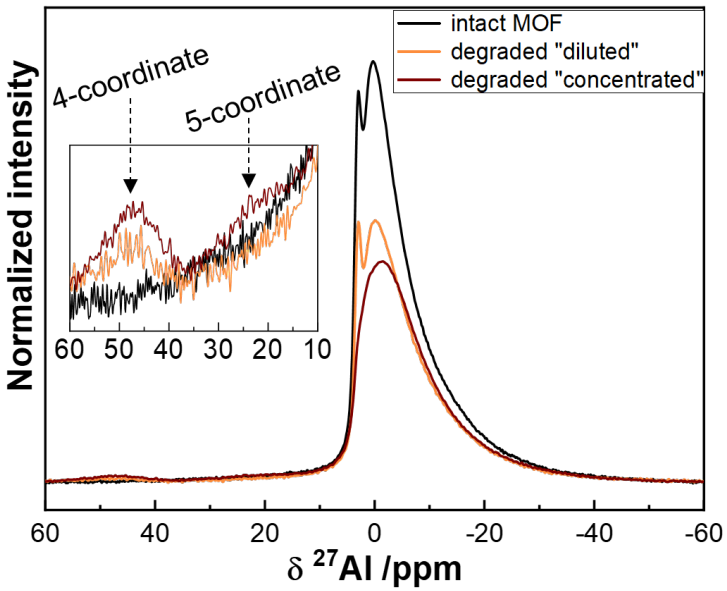


**Figure 6.** $^{27}$Al MAS NMR of the degraded nanoMIL-100Al) at the "diluted" and "concentrated" conditions, demonstrating the effect of increasing P/$Al_3$ ratio on the nanoMOF degradation reaction. The arrows indicate the position of 4- and 5-coordinate Aluminum species

The present ssNMR study about nanoMIL-100(Al) so far agrees with the hypothesis of Li *et al*. about nanoMIL-100(Fe)[37] that aluminum phosphate/iron phosphate complex is the degradation product of nanoMIL-100 reacting with phosphate buffer PBS. While Li *et al*. could only hypothesize the formation of iron phosphate and iron oxide hematite and goethite[37], the present study offers concrete evidence about the structure of the degraded nanoMIL-100(Al) by showing the coordination states of Al and the likely formation of Al-O-P bond in the degradation product.

To summarize, we propose for the first time a molecular mechanism of nanoMIL-100(Al) degradation in the mimicking biological medium PBS as follows (**Figure 7**):

1) Phosphate ions in PBS attack nanoMIL-100(Al) surface, substitute labile water ligands of MIL-100(Al), and form coordination Al-O-P bond with MIL-100(Al). Consequently, the Al-O-C coordination bonds between MIL-100(Al) trimer and trimesate linker are weakened.

2) Phosphate ions substitute carboxylate of trimesate linker. As the substitution of water and trimesate continues, the formation of 6-fold aluminum atoms with a new coordination sphere (i.e., aluminum bonded with 1 to 2 phosphate groups) continues, producing the main degradation products of nanoMIL-100(Al). The release of free trimesic acid starts when all six Al-O-C bonds between a trimesate linker and Al trimers are broken.

3) New 4 and 5-coordinate Al species are produced, most likely as a layer of inorganic aluminum phosphate $AlPO_4$ on the nanoMIL-100(Al) surface, due to cleavage of trimesate linker and the aluminum-oxo center

4) After 6 hours, the insoluble aluminum phosphate species $AlPO_4$ passivate the MOF pore and pore window. The intact trimers of nanoMIL-100(Al) are no longer exposed to a high amount of phosphate. As a result, the degradation reaction reaches equilibrium, and the release of trimesate reaches the maximum.

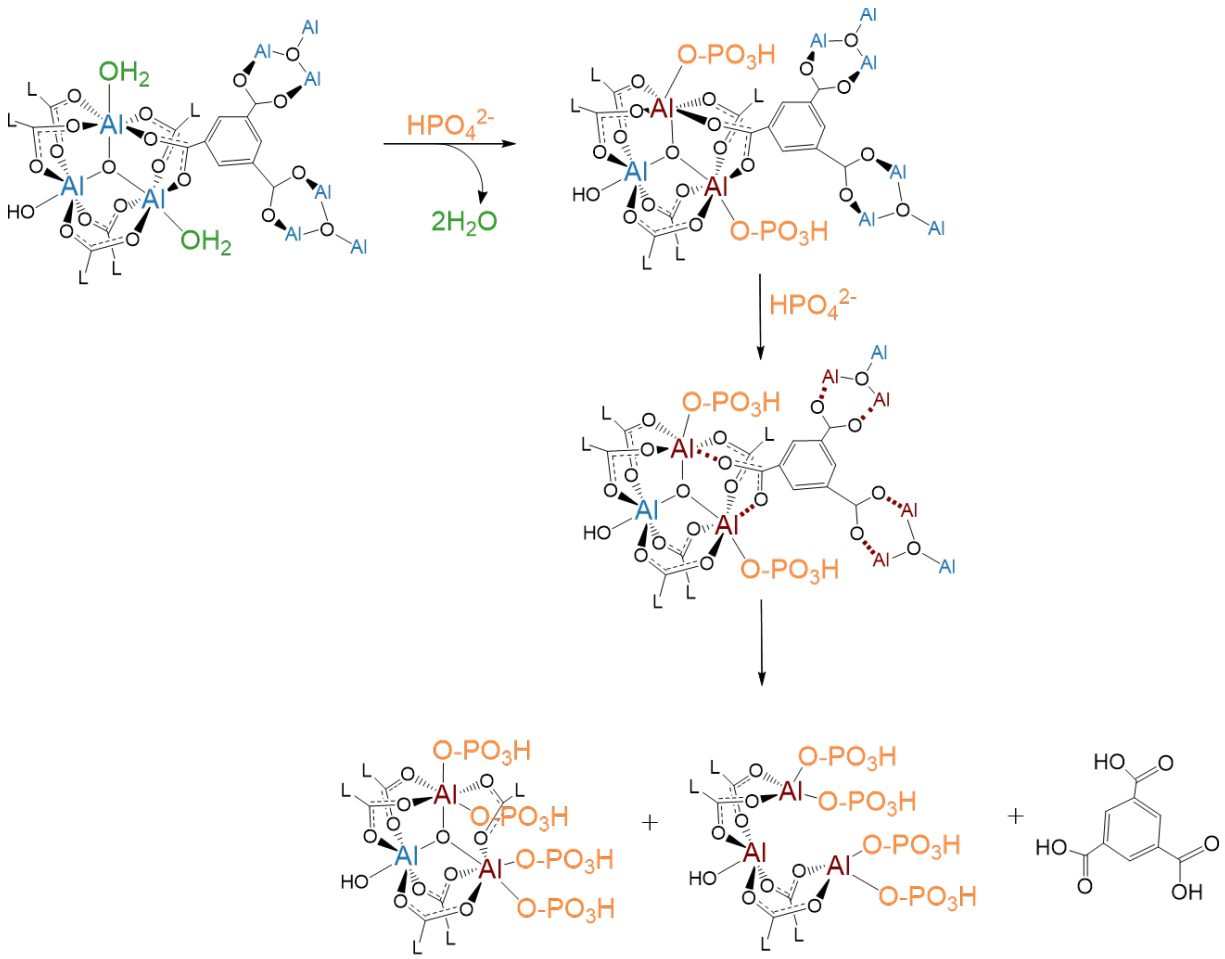


**Figure 7.** Proposed degradation mechanism of nanoMIL-100(Al) in phosphate buffer solution

### 3.3. Degradation mechanism of drug-loaded and surface-coated nanoMIL-100(Al)

In the final step, we analyzed the effect of surface coating and drug loading on the nanoMIL-100(Al) degradation processes. As reported in the literature, the presence of loaded drug and surface coating could alter the physicochemical properties of nanoMOF[21,26], thus potentially affecting nanoMOF's degradation reaction.

NanoMIL-100(Al) was successfully loaded with adenosine triphosphate (ATP) at 18.6 ±0.8 wt%, and coated with β-cyclodextrin-phosphate (CD-P) at 28.3 ± 0.4 wt%. Before studying the degradation, the drug loading and surface coating quality were evaluated. Results of $^{27}$Al and $^{31}$P

MAS NMR in **Figure S14a** and **Figure S14b** agree with our previous study[24]. $^{31}$P MAS NMR (**Figure S16b**) showed that the drug ATP is captured inside MIL-100(Al) by chemical adsorption through Al-O-P coordination. $^{27}$Al MAS NMR (**Figure S16a**) showed that the CD-P coating is located at the surface and does not penetrate the MOF core. The integrity of the trimesate framework was checked by TEM and $^{13}$C MAS NMR, see **Figure S15** and **Figure S17**, respectively. From now on, we denote in the figures below the CD-P-surface-coated nanoMIL-100(Al) as MOF-coated, the ATP-drug-loaded nanoMIL-100(Al) as MOF-loaded, the ATP-drug-loaded-CDP-surface-coated nanoMIL-100(Al) as MOF-loaded-coated.

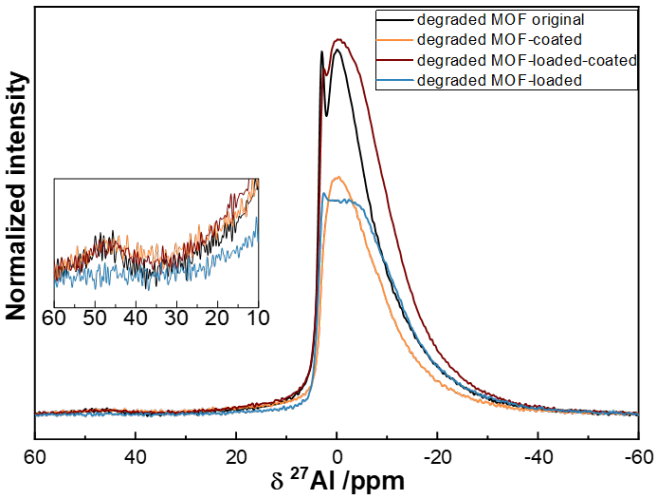


**Figure 8.** $^{27}$Al MAS NMR spectra of degraded original and degraded modified nanoMIL-100(Al), presenting the impact of drug encapsulation and surface coating on the nanoMOF degradation

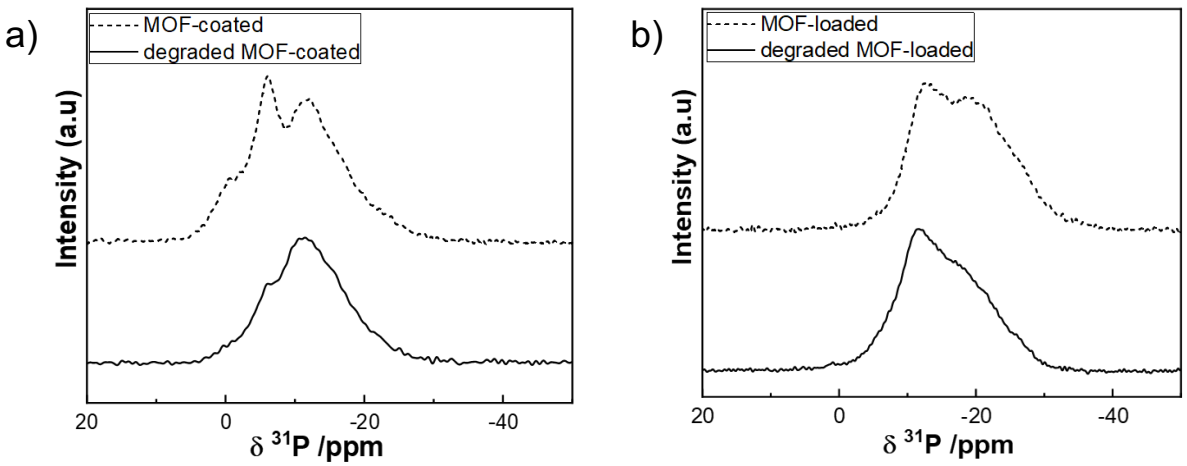


354 **Figure 9.** $^{31}$P MAS NMR of a) degraded CD-P-coated MIL-100(Al) compared to CD-P-coated
355 MIL-100(Al), and b) degraded ATP-loaded-MIL-100(Al) compared to ATP-loaded-MIL-100(Al).
356 CD-P and ATP are still present in the degraded nanoMOF after 4-5 days of degradation

357 Degradation of the CD-P coated nanoMIL-100(Al) is similar to degradation of the non-coated
358 one. In **Figure 8**, the $^{27}$Al MAS NMR spectrum of the degraded MOF-CDP shows both the hexa-
359 coordinate Al-O-P around -2 ppm and the tetra-coordinate aluminophosphate at 48 ppm.
360 Observing a similar degradation product, we speculate that, as CD-P covers approximately 30%
361 of the nanoMIL-100(Al) surface[26], degradation reaction still occurs at the nanoMOF's surface not
362 attached to CD-P, following the reaction mechanism proposed in the previous section.

363 Additionally, the $^{31}$P MAS NMR spectrum of the degraded MOF-CDP in **Figure 9a** displays a
364 shoulder around -10 ppm which belongs to CD-P, and the dominant signal of the phosphate
365 coordinated with the MIL-100(Al) framework around -15 ppm. The presence of CD-P coating
366 even after five days of degradation suggests that CD-P competes with inorganic phosphate ions to
367 complex with Al(III). Consequently, PBS phosphates can only partially displace CD-P.

368 Meanwhile, the degradation reaction of the ATP-loaded nanoMIL-100(Al) exhibits features
369 distinctive from that of the empty nanoMOF. No sign of low-coordinated Al was detected. $^{27}$Al

NMR (**Figure 8**) still showed the 6-coordinate Al species around -2 ppm as the main degradation product, while the Al species bonded with phosphate ATP was still present. Likewise, the $^{31}$P MAS NMR spectrum in **Figure 9b** shows both a peak of coordinated PBS phosphate and a shoulder signal of ATP. Both $^{27}$Al and $^{31}$P NMR data consistently suggest that nanoMIL-100(Al) loaded with ATP is less degraded than the empty one, and only a part of ATP is liberated from the framework. Similar to the surface coating CD-P, the loaded drug ATP competes with inorganic PBS phosphates to coordinate the Al(III) of nanoMIL-100(Al). The triphosphate ATP is a much stronger complexing ligand towards Al(III) than the hydrogen phosphate and dihydrogen phosphate ions[60], meaning that MIL-100(Al) forms a more stable coordination complex with ATP than with phosphate ions. Therefore, it is difficult to break the coordination between ATP and Al(III) by solely phosphate PBS, which explains the presence of ATP in the $^{31}$P NMR spectrum, even after days of degradation. However, the strong Al-O-P bond between Al(III) and ATP makes the Al-O-C bond between Al(III) and trimesate linker more easily attacked by phosphate. We hypothesize that phosphate attacks the Al-O-C bond with trimesate, forming hexa-coordinate Al-O-P in the region -2 to -5 ppm observed in the $^{27}$Al spectrum. When the Al center forms a new coordination bond with inorganic phosphate, its coordination bond with ATP is weakened. As a result, the probability is higher for phosphate to displace ATP from the framework. Another factor to be considered is the steric effect caused by ATP. Bulky ATP possibly hinders phosphate diffusion in the MIL-100(Al) trimer, thus preventing trimesate substitution.

In addition, the notable absence of the low-coordinate aluminophosphate can be explained by the chelating capability of triphosphate ATP[61,62]. ATP coordinates with MIL-100(Al) through the terminal γ-phosphorus. During the breaking of the Al-O-C bond, the β-phosphorus of ATP can compete with phosphate PBS ions and create a second coordination bond with Al. The bidentate

393 Al-ATP coordination not only halts the formation of low-coordinate Al but also prevents the 100%
394 release of ATP. Consistently, only 60% ATP was released in excessive PBS, while 100% of
395 trimesate ligand was found by HPLC (data not shown).
396 Finally, combining the effect of drug encapsulation and surface coating, **Figure 8** shows that
397 degradation of the ATP-loaded CD-P-surface-coated nanoMIL-100(Al) produces both 6-
398 coordinate aluminophosphate complex and 4-coordinate inorganic aluminophosphate, but with a
399 slightly lower proportion of 4-coordinate degraded complex (1.0%) than that in the surface-coated
400 empty nanoMIL-100(Al) (1.6%). Also, the $^{27}$Al peak at 2.5 ppm belonging to the original
401 nanoMIL-100(Al) is more preserved in the degraded one in the presence of the drug ATP.
402 In summary, the degradation reaction of the modified MOF including the ATP-loaded and the
403 CD-P-surface coated nanoMIL100(Al) can be summarized as follows:
404 1) Surface coating with CD-P has a negligible effect on the degradation of nanoMIL-100(Al).
405 6-coordinate and 4-coordinate aluminum complexes with phosphate are formed as described in the
406 degradation mechanism of the original nanoMIL-100(Al)
407 2) Encapsulation of ATP inside nanoMIL-100(Al) impacts significantly the nanoMOF
408 degradation. Degradation of ATP-loaded nanoMIL-100(Al) starts with the substitution of
409 trimesate Al-O-C bond, thus producing hexa-coordinate aluminophosphate and free trimesate.
410 However, the bulky ATP limits the amount of trimesate release. The coordination of PBS
411 phosphate with the Al trimer facilitates the dissociation of the Al-O-P bond with ATP. Then,
412 phosphate from PBS replaces the bonded ATP, leading to the release of free ATP. During the bond
413 dissociation process, the coordinated ATP can make the second coordination bond with the
414 degraded Al trimer. Consequently, no low-coordinated Al is created, and ATP is not entirely
415 released.

3.4. Degradation mechanism of nanoMIL-100(Fe), in comparison with nanoMIL-100(Al)

To evaluate whether our proposed degradation mechanism applies to the iron MIL-100 analog nanoMIL-100(Fe), XANES spectroscopy was used to study the *ex situ* degradation of the original, CD-P surface-coated, and ATP-loaded nanoMIL-100(Fe). Similar to nanoMIL-100(Al), nanoMIL-100(Fe) was incubated in PBS at 37°C, then the degraded nanoparticles were recovered after 48 hours. A "very diluted" condition: 0.5 mg.mL$^{-1}$ nanoMIL-100(Fe) in PBS 10 mM was used to produce as much as possible degraded MIL-100(Fe) species.

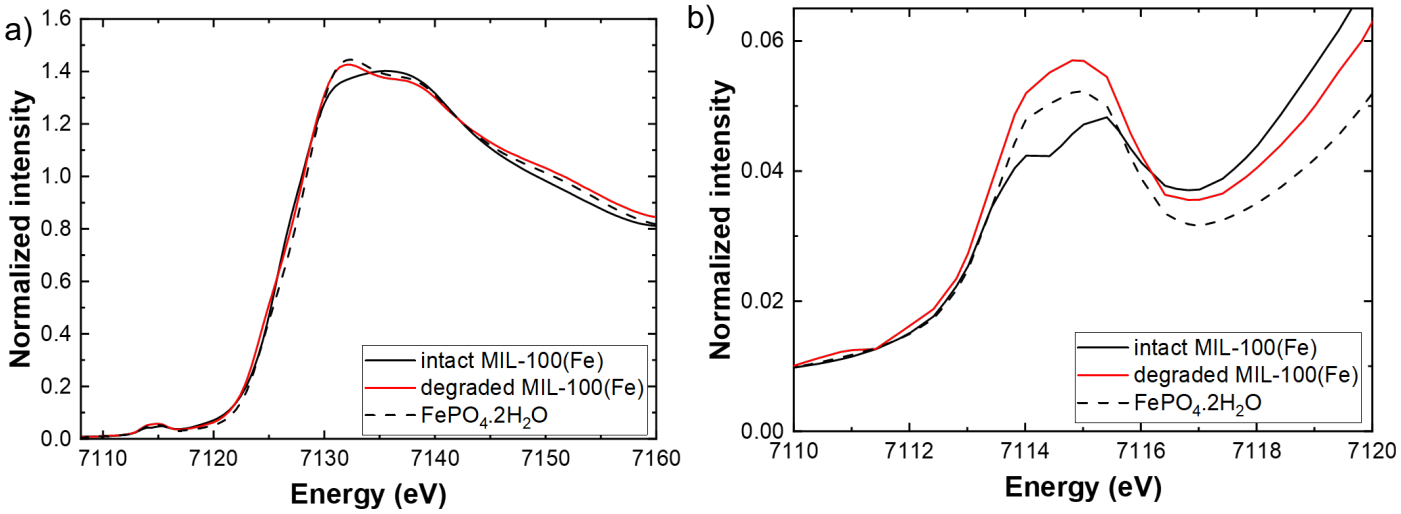


**Figure 10**. a) Normalized Fe K-edge XANES spectra, and b) zoom on pre-edge region of degraded nanoMIL-100(Fe) compared with original nanoMIL-100(Fe) and iron(III) phosphate dihydrate

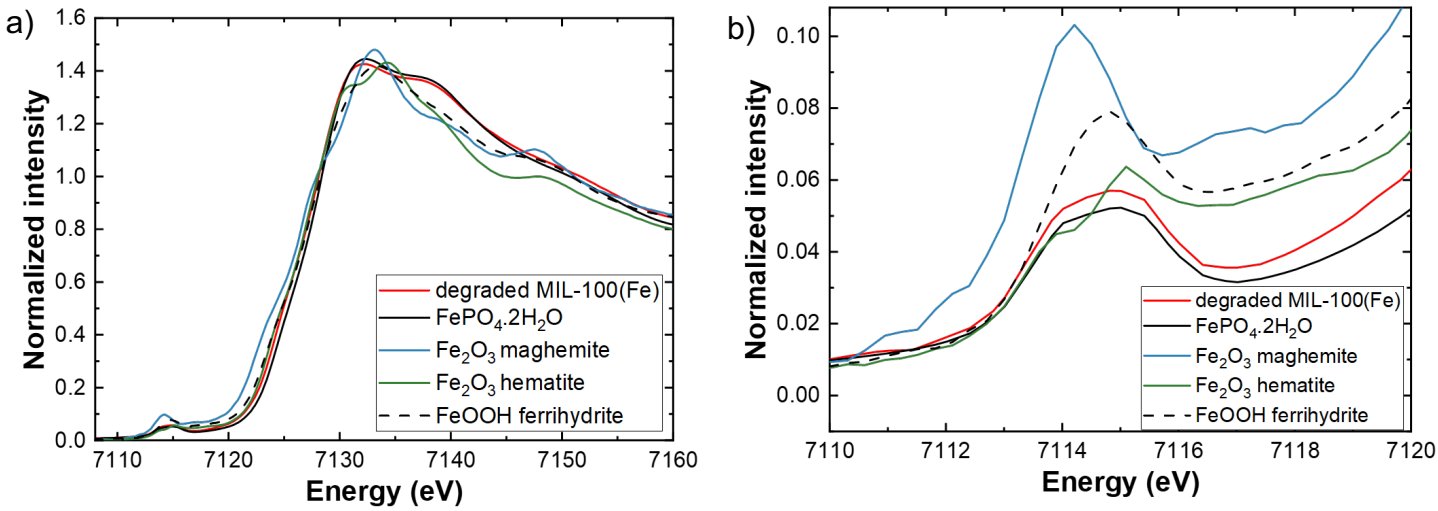


425 **Figure 11.** a) Normalized Fe K-edge XANES spectra, and b) zoom on the pre-edge region of
426 degraded nanoMIL-100(Fe) compared with several Fe(III) possible degradation products, iron
427 phosphate, iron oxides, and iron oxyhydroxide

428 The evolution of original nanoMIL-100(Fe) after degradation is shown in **Figure 10**. The
429 XANES Fe K-edge spectrum of the degraded nanoMIL-100(Fe) is reminiscent of that of iron (III)
430 phosphate dihydrate, a substance having 6-coordinate iron (III) bonds with phosphate through Fe-
431 O-P bond[63]. This similarity is also observed in the pre-edge region, where the intact MIL-100(Fe)
432 shows two features at 7114 and 7115.4 eV, while the degraded MIL-100(Fe) and $FePO_4.2H_2O$
433 only show a single, broad peak at 7114.9 eVc. Moreover, the XANES spectrum of this degraded
434 nanoMIL-100(Fe) is different from those of iron (III) oxide and iron (III) oxyhydroxide, excluding
435 their presence in the degraded nanoMIL-100(Fe) (**Figure 11**). Therefore, we propose that the first
436 step of nanoMIL-100(Fe) degradation also forms an iron-phosphate-6-coordinate species with Fe-
437 O-P coordination bond, in the same way as illustrated in **Figure 7**, where phosphate from PBS
438 replaces water ligand of nanoMIL-100(Fe) and coordinates with Fe(III). The 4-coordinate iron
439 phosphate species were not detected due to its low amount, probably 1% of iron in the degraded
440 nanoMIL-100(Fe). Note that nanoMIL-100(Fe) also became less porous after degradation (**Figure**

**S18**) with a smaller decrease (50% decrease) in the BET surface area than in nanoMIL-100(Al) (90% decrease).

In addition, after degradation reaction, the oxidation number of Fe in nanoMIL-100(Fe) does not change and remain as +III, as the degraded and original nanoMIL-100(Fe) have the same edge position (**Figure 10a**), and the edge position of nanoMIL-100(Fe) is close to the values of Fe(III) compounds (**Figure S19**). Previously observed by other authors using Mossbauer spectroscopy[37], this maintenance of Fe oxidation number after nanoMIL-100(Fe) degradation is consistent with our proposed degradation mechanism based on the model nanoMIL-100(Al) (**Figure 7**) which describes degradation as an acid-base reaction.

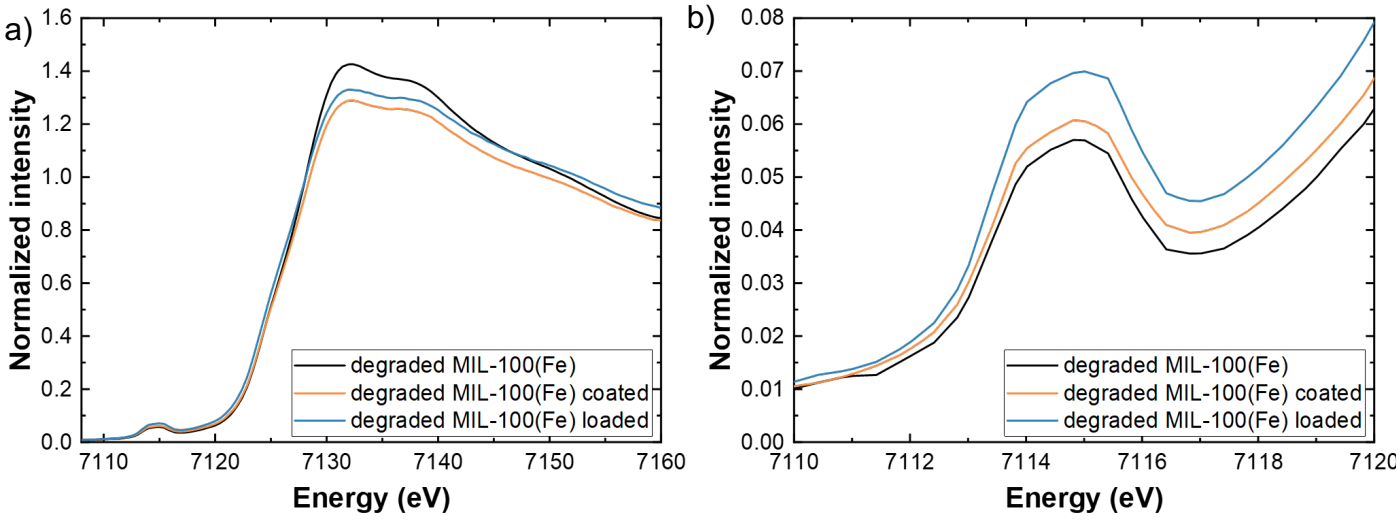


**Figure 12**. a) Normalized Fe K-edge XANES spectra of degraded original and modified nanoMIL-100(Fe), and b) zoom on the pre-edge region

The effect of ATP drug loading and CD-P surface coating on the nanoMIL-100(Fe) degradation was also investigated. **Figure S20** shows that the ATP-drug-loaded and CD-P-surface-coated nanoMIL-100(Fe) share the same XANES features as the original one, indicating that drug loading and surface coating do not degrade nanoMIL-100(Fe). **Figure 12** shows that degradation of drug-loaded, and surface-coated nanoMIL-100(Fe) produces similar species as obtained from

457 degradation of original one, as all three XANES and pre-edge spectra have similar shapes and
458 features. Once again, XANES spectroscopy shows that 6-coordinate iron-phosphate was formed
459 during the degradation reaction of nanoMIL-100(Fe).
460 This complementary study with XANES suggests that the first step in degradation of nanoMIL-
461 100(Fe) likely follows the degradation reaction of its aluminum analog, corroborating the ssNMR
462 study on nanoMIL-100(Al).
463
464 4. Conclusions
465 By using solid-state NMR spectroscopy, we obtained novel knowledge about the degradation
466 mechanism of nanoMIL-100(Al) and nanoMIL-100(Fe) in phosphate buffer. For the first time, we
467 find direct evidence about the change of the metal coordination sphere and the limiting reaction
468 step in the nanoMIL-100 degradation mechanism. First, upon substitution of labile water ligands
469 by phosphate, Al-O-P coordination bonds are formed between aluminum species at the surface of
470 nanoMOF and phosphate from the medium, creating 6-coordinate aluminophosphate. Second, the
471 substitution of trimesate by phosphate leads to the release of free trimesate and creates 4-coordinate
472 inorganic aluminum phosphate. This 4-coordinate aluminum, which has not been observed before,
473 can passivate the nanoMOF surface and slow down the degradation reaction. Additionally, our
474 study demonstrates that chemical modification such as drug encapsulation and surface coating can
475 impact the nanoMOF degradation, hence its drug release process, as a function of metal-ligand
476 bond strength.
477 To conclude, insights about the degradation mechanism of nanoMOF from this work contribute
478 to the understanding of MOF chemistry and help optimize the performance of nanoMOF drug
479 carriers. This study also highlights the useful role of ssNMR spectroscopy with the support of

XANES spectroscopy in investigating in depth the nanoMOF structure. Using ssNMR spectroscopy, we were able to obtain enough evidence about the coordination sphere and the reaction limiting step of nanoMIL-100(Al) degradation, whilst XANES spectroscopy provided complementary proof on the reaction of nanoMIL-100(Fe). The obtained knowledge in this study prompts new studies on understanding drug delivery chemistry and developing characterization tools for drug nanocarrier. Comparative studies of MIL-100(Al) and MIL-100(Fe) are being carried out to investigate the behaviors of MIL-100 analogs. Various types of drug compounds can be explored when different host-guest interactions and degradation behaviors are expected. In the future, we will develop a new NMR spectroscopy method to monitor *in situ* drug delivery processes of nanoMOF.

## ASSOCIATED CONTENT

**Supporting Information**. The supporting information contains: 1) experimental procedures of nanoMOF preparation and characterization, 2) standard characterization of nanoMIL-100(Al): DLS, TEM, XRD, BET, TGA, $^{1}$H MAS NMR, $^{13}$C MAS NMR, $^{27}$Al MAS and MQMAS NMR spectra, 3) complementary NMR measurements on degraded nanoMIL-100(Al):, $^{31}$P, $^{1}$H-$^{31}$P, $^{1}$H-$^{27}$Al. The file is available free of charge *via* the Internet at http://pubs.acs.org

## AUTHOR INFORMATION

**Corresponding Authors**

Charlotte Martineau-Corcos, ccorcos@cortecnet.com, Orcid: 0000-0003-1887-1042

Ruxandra Gref, ruxandra.gref@universite-paris-saclay.fr, Orcid : 0000-0002-7869-0908

**Authors**

Mai Dang Le Vuong

Ioanna Christodoulou

Marianna Porcino

Si-Thanh Dong

Benedikt Lassalle-Kaiser

Mohamed Haouas

**Present Addresses**

(a) Université Paris-Saclay, UVSQ, CNRS, Institut Lavoisier de Versailles, 78000, Versailles, France

(b) CortecNet, 7 avenue du Hoggar, 91940 Les Ulis, France

**Author Contributions**

C.M.C. and R.G. conceived the idea and designed the experiments. M.V. and I.C. synthesized and characterized the materials. M.P. performed the high field MAS NMR spectroscopy experiments. M.V., B.L-K., and S-T.D. performed and analyzed XANES spectroscopy measurement. M.V. and C.M.C. analyzed data. All authors participated in the data discussion. M.V. wrote the manuscript, and all authors revised the manuscript. All authors have approved the final version of the manuscript.

## Notes

The authors declare no competing financial interest.


## ACKNOWLEDGMENT

Financial support from the IR-RMN-THC Fr3050 CNRS for conducting the research is gratefully acknowledged. This work was also supported by the Paris Ile-de-France Region – DIM "Respore". The present work has benefited from Imagerie-Gif core facility supported by l'Agence Nationale de la Recherche (ANR-11-EQPX-0029/Morphoscope, ANR-10-INBS-04/FranceBioImaging; ANR-11-IDEX-0003-02/ Saclay Plant Sciences). We also thank the beamline scientists and staffs at the SAMBA beamline for assistance. MP and CMC thank Dr. Vincent Sarou-Kanian (CEMHTI Orléans) for support during the high-field NMR experiments.


## REFERENCES


(1) Folkman, J.; Long, D. M. The Use of Silicone Rubber as a Carrier for Prolonged Drug Therapy. *J. Surg. Res.* **1964**, *4*, 139–142. DOI: 10.1016/S0022-4804(64)80040-8.

(2) Horcajada, P.; Chalati, T.; Serre, C.; Gillet, B.; Sebrie, C.; Baati, T.; Eubank, J. F.; Heurtaux, D.; Clayette, P.; Kreuz, C.; *et al*. Porous Metal–Organic-Framework Nanoscale Carriers as a Potential Platform for Drug Delivery and Imaging. *Nat. Mater.* **2010**, *9*, 172–178. DOI: 10.1038/nmat2608

(3) Férey, G. Hybrid Porous Solids: Past, Present, Future. *Chem. Soc. Rev.* **2007**, *37*, 191–214. DOI: 10.1039/B618320B.

(4) Furukawa, H.; Cordova, K. E.; O'Keeffe, M.; Yaghi, O. M. The Chemistry and Applications of Metal-Organic Frameworks. *Science* **2013**, *341*, 1230444. DOI: 10.1126/science.1230444.

(5) Horike, S.; Shimomura, S.; Kitagawa, S. Soft Porous Crystals. *Nat. Chem.* **2009**, *1*, 695–704. DOI: 10.1038/nchem.444.

(6) Horcajada, P.; Surblé, S.; Serre, C.; Hong, D.-Y.; Seo, Y.-K.; Chang, J.-S.; Grenèche, J.-M.; Margiolaki, I.; Férey, G. Synthesis and Catalytic Properties of MIL-100(Fe), an Iron(III) Carboxylate with Large Pores. *Chem. Commun.* **2007**, No. 27, 2820–2822. DOI: 10.1039/B704325B.

(7) Volkringer, C.; Popov, D.; Loiseau, T.; Férey, G.; Burghammer, M.; Riekel, C.; Haouas, M.; Taulelle, F. Synthesis, Single-Crystal X-Ray Microdiffraction, and NMR Characterizations of the Giant Pore Metal-Organic Framework Aluminum Trimesate MIL-100. *Chem. Mater.* **2009**, *21*, 5695–5697. DOI: 10.1021/cm901983a.
(8) Agostoni, V.; Horcajada, P.; Rodriguez-Ruiz, V.; Willaime, H.; Couvreur, P.; Serre, C.; Gref, R. 'Green' Fluorine-Free Mesoporous Iron(III) Trimesate Nanoparticles for Drug Delivery. *Green Mater.* **2013**, *1*, 209–217. DOI: 10.1680/gmat.13.00001.
(9) Kökçam-Demir, Ü.; Goldman, A.; Esrafili, L.; Gharib, M.; Morsali, A.; Weingart, O.; Janiak, C. Coordinatively Unsaturated Metal Sites (Open Metal Sites) in Metal–Organic Frameworks: Design and Applications. *Chem. Soc. Rev.* **2020**, *49*, 2751–2798. DOI: 10.1039/C9CS00609E.
(10) Vitillo, J. G.; Gagliardi, L. Thermal Treatment Effect on CO and NO Adsorption on Fe(II) and Fe(III) Species in Fe3O-Based MIL-Type Metal–Organic Frameworks: A Density Functional Theory Study. *Inorg. Chem.* **2021**, *60*, 11813–11824. DOI: 10.1021/acs.inorgchem.1c01044.
(11) Christodoulou, I.; Bourguignon, T.; Li, X.; Patriarche, G.; Serre, C.; Marlière, C.; Gref, R. Degradation Mechanism of Porous Metal-Organic Frameworks by In Situ Atomic Force Microscopy. *Nanomaterials* **2021**, *11*, 722. DOI: 10.3390/nano11030722.
(12) Horcajada, P.; Gref, R.; Baati, T.; Allan, P. K.; Maurin, G.; Couvreur, P.; Férey, G.; Morris, R. E.; Serre, C. Metal–Organic Frameworks in Biomedicine. *Chem. Rev.* **2012**, *112*, 1232–1268. DOI: 10.1021/cr200256v.
(13) Quijia, C. R.; Lima, C.; Silva, C.; Alves, R. C.; Frem, R.; Chorilli, M. Application of MIL-100(Fe) in Drug Delivery and Biomedicine. *J. Drug Delivery Sci. Technol.* **2021**, *61*, 102217. DOI: 10.1016/j.jddst.2020.102217.
(14) Rodriguez-Ruiz, V.; Maksimenko, A.; Anand, R.; Monti, S.; Agostoni, V.; Couvreur, P.; Lampropoulou, M.; Yannakopoulou, K.; Gref, R. Efficient "Green" Encapsulation of a Highly Hydrophilic Anticancer Drug in Metal–Organic Framework Nanoparticles. *J. Drug Targeting* **2015**, *23*, 759–767. DOI: 10.3109/1061186X.2015.1073294.
(15) Li, X.; Salzano, G.; Qiu, J.; Menard, M.; Berg, K.; Theodossiou, T.; Ladavière, C.; Gref, R. Drug-Loaded Lipid-Coated Hybrid Organic-Inorganic "Stealth" Nanoparticles for Cancer Therapy. *Front. Bioeng. Biotechnol.* **2020**, *8*, 1027. DOI: 10.3389/fbioe.2020.01027.
(16) Unamuno, X.; Imbuluzqueta, E.; Salles, F.; Horcajada, P.; Blanco-Prieto, M. J. Biocompatible Porous Metal-Organic Framework Nanoparticles Based on Fe or Zr for Gentamicin Vectorization. *Eur. J. Pharm. Biopharm.* **2018**, *132*, 11–18. DOI: 10.1016/j.ejpb.2018.08.013.
(17) Li, X.; Semiramoth, N.; Hall, S.; Tafani, V.; Josse, J.; Laurent, F.; Salzano, G.; Foulkes, D.; Brodin, P.; Majlessi, L.; *et al*. Compartmentalized Encapsulation of Two Antibiotics in Porous Nanoparticles: An Efficient Strategy to Treat Intracellular Infections. *Part. Part. Syst. Charact.* **2019**, *36*, 1800360. DOI: 10.1002/ppsc.201800360.
(18) Agostoni, V.; Chalati, T.; Horcajada, P.; Willaime, H.; Anand, R.; Semiramoth, N.; Baati, T.; Hall, S.; Maurin, G.; Chacun, H.; *et al*. Towards an Improved Anti-HIV Activity of NRTI via Metal–Organic Frameworks Nanoparticles. *Adv. Healthcare Mater.* **2013**, *2*, 1630–1637. DOI: 10.1002/adhm.201200454.

(19) Taherzade, S. D.; Rojas, S.; Soleimannejad, J.; Horcajada, P. Combined Cutaneous Therapy Using Biocompatible Metal-Organic Frameworks. *Nanomaterials* **2020**, *10*, 2296. DOI: 10.3390/nano10122296.
(20) Chalati, T.; Horcajada, P.; Couvreur, P.; Serre, C.; Ben Yahia, M.; Maurin, G.; Gref, R. Porous Metal Organic Framework Nanoparticles to Address the Challenges Related to Busulfan Encapsulation. *Nanomedicine* **2011**, *6*, 1683–1695. DOI: 10.2217/nnm.11.69.
(21) Simon-Yarza, M. T.; Baati, T.; Paci, A.; Lesueur, L. L.; Seck, A.; Chiper, M.; Gref, R.; Serre, C.; Couvreur, P.; Horcajada, P. Antineoplastic Busulfan Encapsulated in a Metal Organic Framework Nanocarrier: First in Vivo Results. *J. Mater. Chem. B* **2016**, *4*, 585–588. DOI: 10.1039/C5TB02084K.
(22) Feng, Y.; Wang, C.; Ke, F.; Zang, J.; Zhu, J. MIL-100(Al) Gels as an Excellent Platform Loaded with Doxorubicin Hydrochloride for PH-Triggered Drug Release and Anticancer Effect. *Nanomaterials* **2018**, *8*, 446. DOI: 10.3390/nano8060446.
(23) Li, X.; Porcino, M.; Qiu, J.; Constantin, D.; Martineau-Corcos, C.; Gref, R. Doxorubicin-Loaded Metal-Organic Frameworks Nanoparticles with Engineered Cyclodextrin Coatings: Insights on Drug Location by Solid State NMR Spectroscopy. *Nanomaterials* **2021**, *11*, 945. DOI: 10.3390/nano11040945.
(24) Porcino, M.; Christodoulou, I.; Vuong, M. D. L.; Gref, R.; Martineau-Corcos, C. New Insights on the Supramolecular Structure of Highly Porous Core–Shell Drug Nanocarriers Using Solid-State NMR Spectroscopy. *RSC Adv.* **2019**, *9*, 32472–32475. DOI: 10.1039/C9RA07383C.
(25) Giménez-Marqués, M.; Bellido, E.; Berthelot, T.; Simón-Yarza, T.; Hidalgo, T.; Simón-Vázquez, R.; González-Fernández, Á.; Avila, J.; Asensio, M. C.; Gref, R.; *et al.* GraftFast Surface Engineering to Improve MOF Nanoparticles Furtiveness. *Small* **2018**, *14*, 1801900. DOI: 10.1002/smll.201801900.
(26) Agostoni, V.; Horcajada, P.; Noiray, M.; Malanga, M.; Aykaç, A.; Jicsinszky, L.; Vargas-Berenguel, A.; Semiramoth, N.; Daoud-Mahammed, S.; Nicolas, V.; *et al.* A "Green" Strategy to Construct Non-Covalent, Stable and Bioactive Coatings on Porous MOF Nanoparticles. *Sci. Rep.* **2015**, *5*, 1–7. DOI: 10.1038/srep07925.
(27) Cutrone, G.; Qiu, J.; Menendez-Miranda, M.; Casas-Solvas, J. M.; Aykaç, A.; Li, X.; Foulkes, D.; Moreira-Alvarez, B.; Encinar, J. R.; Ladavière, C.; *et al.* Comb-like Dextran Copolymers: A Versatile Strategy to Coat Highly Porous MOF Nanoparticles with a PEG Shell. *Carbohydr. Polym.* **2019**, *223*, 115085. DOI: 10.1016/j.carbpol.2019.115085.
(28) Hidalgo, T.; Giménez-Marqués, M.; Bellido, E.; Avila, J.; Asensio, M. C.; Salles, F.; Lozano, M. V.; Guillevic, M.; Simón-Vázquez, R.; González-Fernández, A.; *et al.* Chitosan-Coated Mesoporous MIL-100(Fe) Nanoparticles as Improved Bio-Compatible Oral Nanocarriers. *Sci. Rep.* **2017**, *7*, 43099. DOI: 10.1038/srep43099.
(29) Bellido, E.; Hidalgo, T.; Lozano, M. V.; Guillevic, M.; Simón-Vázquez, R.; Santander-Ortega, M. J.; González-Fernández, Á.; Serre, C.; Alonso, M. J.; Horcajada, P. Heparin-Engineered Mesoporous Iron Metal-Organic Framework Nanoparticles: Toward Stealth Drug Nanocarriers. *Adv. Healthcare Mater.* **2015**, *4*, 1246–1257. DOI: 10.1002/adhm.201400755.
(30) Aykaç, A.; Noiray, M.; Malanga, M.; Agostoni, V.; Casas-Solvas, J. M.; Fenyvesi, É.; Gref, R.; Vargas-Berenguel, A. A Non-Covalent "Click Chemistry" Strategy to Efficiently Coat Highly Porous MOF Nanoparticles with a Stable Polymeric Shell.

*Biochim. Biophys. Acta, Gen. Subj.* **2017**, *1861*, 1606–1616. DOI: 10.1016/j.bbagen.2017.01.016.

(31) Qiu, J.; Li, X.; Rezaei, M.; Patriarche, G.; Casas-Solvas, J. M.; Moreira-Alvarez, B.; Costa Fernandez, J. M.; Encinar, J. R.; Savina, F.; Picton, L.; *et al*. Porous Nanoparticles with Engineered Shells Release Their Drug Cargo in Cancer Cells. *Int. J. Pharm.* **2021**, *610*, 121230. DOI: 10.1016/j.ijpharm.2021.121230.

(32) Ruyra, À.; Yazdi, A.; Espín, J.; Carné-Sánchez, A.; Roher, N.; Lorenzo, J.; Imaz, I.; Maspoch, D. Synthesis, Culture Medium Stability, and In Vitro and In Vivo Zebrafish Embryo Toxicity of Metal-Organic Framework Nanoparticles. *Chem. - Eur. J.* **2015**, *21*, 2508–2518. DOI: 10.1002/chem.201405380.

(33) Grall, R.; Hidalgo, T.; Delic, J.; Garcia-Marquez, A.; Chevillard, S.; Horcajada, P. In Vitro Biocompatibility of Mesoporous Metal (III; Fe, Al, Cr) Trimesate MOF Nanocarriers. *J. Mater. Chem. B* **2015**, *3*, 8279–8292. DOI: 10.1039/C5TB01223F.

(34) Baati, T.; Njim, L.; Neffati, F.; Kerkeni, A.; Bouttemi, M.; Gref, R.; Najjar, M. F.; Zakhama, A.; Couvreur, P.; Serre, C.; *et al*. In Depth Analysis of the in Vivo Toxicity of Nanoparticles of Porous Iron(III) Metal–Organic Frameworks. *Chem. Sci.* **2013**, *4*, 1597–1607. DOI: 10.1039/C3SC22116D.

(35) Simon-Yarza, T.; Baati, T.; Neffati, F.; Njim, L.; Couvreur, P.; Serre, C.; Gref, R.; Najjar, M. F.; Zakhama, A.; Horcajada, P. In Vivo Behavior of MIL-100 Nanoparticles at Early Times after Intravenous Administration. *Int. J. Pharm.* **2016**, *511*, 1042–1047. DOI: 10.1016/j.ijpharm.2016.08.010.

(36) Bellido, E.; Guillevic, M.; Hidalgo, T.; Santander-Ortega, M. J.; Serre, C.; Horcajada, P. Understanding the Colloidal Stability of the Mesoporous MIL-100(Fe) Nanoparticles in Physiological Media. *Langmuir* **2014**, *30*, 5911–5920. DOI: 10.1021/la5012555.

(37) Li, X.; Lachmanski, L.; Safi, S.; Sene, S.; Serre, C.; Grenèche, J. M.; Zhang, J.; Gref, R. New Insights into the Degradation Mechanism of Metal-Organic Frameworks Drug Carriers. *Sci. Rep.* **2017**, *7*, 13142. DOI: 10.1038/s41598-017-13323-1.

(38) Bryce, D. L. NMR Crystallography: Structure and Properties of Materials from Solid-State Nuclear Magnetic Resonance Observables. *IUCrJ* **2017**, *4*, 350–359. DOI: 10.1107/S2052252517006042.

(39) Lucier, B. E. G.; Chen, S.; Huang, Y. Characterization of Metal–Organic Frameworks: Unlocking the Potential of Solid-State NMR. *Acc. Chem. Res.* **2018**, *51*, 319–330. DOI: 10.1021/acs.accounts.7b00357.

(40) Brunner, E.; Rauche, M. Solid-State NMR Spectroscopy: An Advancing Tool to Analyse the Structure and Properties of Metal–Organic Frameworks. *Chem. Sci.* **2020**, *11*, 4297–4304. DOI: 10.1039/D0SC00735H.

(41) Xu, J.; Terskikh, V. V.; Huang, Y. Resolving Multiple Non-Equivalent Metal Sites in Magnesium-Containing Metal-Organic Frameworks by Natural Abundance $^{25}$ Mg Solid-State NMR Spectroscopy. *Chem. - Eur. J.* **2013**, *19*, 4432–4436. DOI: 10.1002/chem.201300113.

(42) Cooper, L.; Guillou, N.; Martineau, C.; Elkaim, E.; Taulelle, F.; Serre, C.; Devic, T. ZrIV Coordination Polymers Based on a Naturally Occurring Phenolic Derivative. *Eur. J. Inorg. Chem.* **2014**, *2014*, 6281–6289. DOI: 10.1002/ejic.201402891.

(43) Sin, M.; Kavoosi, N.; Rauche, M.; Pallmann, J.; Paasch, S.; Senkovska, I.; Kaskel, S.; Brunner, E. In Situ 13C NMR Spectroscopy Study of CO2/CH4 Mixture Adsorption by

Metal–Organic Frameworks: Does Flexibility Influence Selectivity? *Langmuir* **2019**, *35*, 3162–3170. DOI: 10.1021/acs.langmuir.8b03554.
(44) Cadiau, A.; Lee, J. S.; Borges, D. D.; Fabry, P.; Devic, T.; Wharmby, M. T.; Martineau, C.; Foucher, D.; Taulelle, F.; Jun, C.-H.; *et al*. Design of Hydrophilic Metal Organic Framework Water Adsorbents for Heat Reallocation. *Adv. Mater.* **2015**, *27*, 4775–4780. DOI: 10.1002/adma.201502418.
(45) Skorupska, E.; Jeziorna, A.; Paluch, P.; Potrzebowski, M. J. Ibuprofen in Mesopores of Mobil Crystalline Material 41 (MCM-41): A Deeper Understanding. *Mol. Pharmaceutics* **2014**, *11*, 1512–1519. DOI: 10.1021/mp400670f.
(46) Azaïs, T.; Laurent, G.; Panesar, K.; Nossov, A.; Guenneau, F.; Sanfeliu Cano, C.; Tourné-Péteilh, C.; Devoisselle, J.-M.; Babonneau, F. Implication of Water Molecules at the Silica–Ibuprofen Interface in Silica-Based Drug Delivery Systems Obtained through Incipient Wetness Impregnation. *J. Phys. Chem. C* **2017**, *121*, 26833–26839. DOI: 10.1021/acs.jpcc.7b08919.
(47) Azaïs, T.; Tourné-Péteilh, C.; Aussenac, F.; Baccile, N.; Coelho, C.; Devoisselle, J.-M.; Babonneau, F. Solid-State NMR Study of Ibuprofen Confined in MCM-41 Material. *Chem. Mater.* **2006**, *18*, 6382–6390. DOI: 10.1021/cm061551c.
(48) Porcino, M.; Li, X.; Gref, R.; Martineau-Corcos, C. Solid-State NMR Spectroscopy: A Key Tool to Unravel the Supramolecular Structure of Drug Delivery Systems. *Molecules* **2021**, *26*, 4142. DOI: 10.3390/molecules26144142.
(49) Čendak, T.; Žunkovič, E.; Godec, T. U.; Mazaj, M.; Logar, N. Z.; Mali, G. Indomethacin Embedded into MIL-101 Frameworks: A Solid-State NMR Study. *J. Phys. Chem. C* **2014**, *118*, 6140–6150. DOI: 10.1021/jp412566p.
(50) Sciortino, L.; Alessi, A.; Messina, F.; Buscarino, G.; Gelardi, F. M. Structure of the FeBTC Metal–Organic Framework: A Model Based on the Local Environment Study. *J. Phys. Chem. C* **2015**, *119*, 7826–7830. DOI: 10.1021/acs.jpcc.5b01336.
(51) Du, M.; Li, L.; Li, M.; Si, R. Adsorption Mechanism on Metal Organic Frameworks of Cu-BTC, Fe-BTC and ZIF-8 for CO2 Capture Investigated by X-Ray Absorption Fine Structure. *RSC Adv.* **2016**, *6*, 62705–62716. DOI: 10.1039/C6RA07582G.
(52) Márquez, A. G.; Demessence, A.; Platero-Prats, A. E.; Heurtaux, D.; Horcajada, P.; Serre, C.; Chang, J.-S.; Férey, G.; Peña-O'Shea, V. A. de la; Boissière, C.; *et al*. Green Microwave Synthesis of MIL-100(Al, Cr, Fe) Nanoparticles for Thin-Film Elaboration. *Eur. J. Inorg. Chem.* **2012**, *2012*, 5165–5174. DOI: 10.1002/ejic.201200710.
(53) Menegollo, M.; Tessari, I.; Bubacco, L.; Szabadkai, G. Determination of ATP, ADP, and AMP Levels by Reversed-Phase High-Performance Liquid Chromatography in Cultured Cells. In *Calcium Signalling*; Methods in Molecular Biology; Vol. 1925, Humana, New York, NY, 2019; pp 223–232. DOI: 10.1007/978-1-4939-9018-4_19.
(54) Malvern Panalytical. *An Introduction to Dynamic Light Scattering (DLS)*.
(55) Haouas, M.; Volkringer, C.; Loiseau, T.; Férey, G.; Taulelle, F. Monitoring the Activation Process of the Giant Pore MIL-100(Al) by Solid State NMR. *J. Phys. Chem. C* **2011**, *115*, 17934–17944. DOI: 10.1021/jp206513v.
(56) Haouas, M.; Taulelle, F.; Martineau, C. Recent Advances in Application of 27Al NMR Spectroscopy to Materials Science. *Prog. Nucl. Magn. Reson. Spectrosc.* **2016**, *94–95*, 11–36. DOI: 10.1016/j.pnmrs.2016.01.003.

(57) Mortlock, R. F.; Bell, A. T.; Radke, C. J. Phosphorus-31 and Aluminum-27 NMR Investigations of the Effects of pH on Aqueous Solutions Containing Aluminum and Phosphorus. *J. Phys. Chem.* **1993**, *97*, 775–782. DOI: 10.1021/j100105a040.

(58) Mooney, R. C. L. The Crystal Structure of Aluminium Phosphate and Gallium Phosphate, Low-Cristobalite Type. *Acta Crystallogr.* **1956**, *9*, 728–734. DOI: 10.1107/S0365110X56001996.

(59) Müller, D.; Jahn, E.; Ladwig, G.; Haubenreisser, U. High-Resolution Solid-State 27Al and 31P NMR: Correlation between Chemical Shift and Mean Al-O-P Angle in AlPO4 Polymorphs. *Chem. Phys. Lett.* **1984**, *109*, 332–336. DOI: 10.1016/0009-2614(84)85596-7.

(60) Atkári, K.; Kiss, T.; Bertani, R.; Martin, R. B. Interactions of Aluminum(III) with Phosphates. *Inorg. Chem.* **1996**, *35*, 7089–7094. DOI: 10.1021/ic960329e.

(61) Karlik, S. J.; Elgavish, G. A.; Eichhorn, G. L. Multinuclear NMR Studies on Aluminum(III) Complexes of ATP and Related Compounds. *J. Am. Chem. Soc.* **1983**, *105*, 602–609. DOI: 10.1021/ja00341a047.

(62) Khan, M. M. T.; Martell, A. E. Metal Chelates of Adenosine Triphosphate. *J. Phys. Chem.* **1962**, *66*, 10–15. DOI: 10.1021/j100807a003.

(63) Song, Y.; Zavalij, P. Y.; Suzuki, M.; Whittingham, M. S. New Iron(III) Phosphate Phases: Crystal Structure and Electrochemical and Magnetic Properties. *Inorg. Chem.* **2002**, *41*, 5778–5786. DOI: 10.1021/ic025688q.

## TABLE OF CONTENTS GRAPHIC

*For table of content only*